

## Article

# Fabrication of Pt-Loaded Catalysts Supported on the Functionalized Pyrolytic Activated Carbon Derived from Waste Tires for the High Performance Dehydrogenation of Methylcyclohexane and Hydrogen Production

Hongli Ye <sup>1,2,3</sup> , Tianci Wang <sup>3,4</sup>, Shuangxi Liu <sup>3,4</sup>, Cui Zhang <sup>3,4,\*</sup>  and Youqiong Cai <sup>1,2,\*</sup>

- <sup>1</sup> Laboratory of Aquatic Product Quality, Safety and Processing, East China Sea Fisheries Research Institute, Chinese Academy of Fishery Sciences, Shanghai 200090, China; yehongli12@163.com
- <sup>2</sup> Key Laboratory of Control of Safety and Quality for Aquatic Product, Ministry of Agriculture and Rural Affairs, Beijing 100141, China
- <sup>3</sup> Institute of New Catalytic Materials Science and MOE Key Laboratory of Advanced Energy Materials Chemistry, School of Materials Science and Engineering, National Institute of Advanced Materials, Nankai University, Tianjin 300350, China; 2120190957@mail.nankai.edu.cn (T.W.); sxliu@nankai.edu.cn (S.L.)
- <sup>4</sup> Collaborative Innovation Center of Chemical Science and Engineering (Tianjin), Tianjin 300072, China
- \* Correspondence: zhangcui@nankai.edu.cn (C.Z.); caiyouqiong@163.com (Y.C.)



**Citation:** Ye, H.; Wang, T.; Liu, S.; Zhang, C.; Cai, Y. Fabrication of Pt-Loaded Catalysts Supported on the Functionalized Pyrolytic Activated Carbon Derived from Waste Tires for the High Performance Dehydrogenation of Methylcyclohexane and Hydrogen Production. *Catalysts* **2022**, *12*, 211. <https://doi.org/10.3390/catal12020211>

Academic Editors: Elti Cattaruzza, Alberto Vomiero and Francesco Enrichi

Received: 13 January 2022

Accepted: 6 February 2022

Published: 11 February 2022

**Publisher's Note:** MDPI stays neutral with regard to jurisdictional claims in published maps and institutional affiliations.



**Copyright:** © 2022 by the authors. Licensee MDPI, Basel, Switzerland. This article is an open access article distributed under the terms and conditions of the Creative Commons Attribution (CC BY) license (<https://creativecommons.org/licenses/by/4.0/>).

**Abstract:** The pyrolytic activated carbon derived from waste tires (PTC) was functionalized to fabricate the high performance of Pt-based catalysts in the dehydrogenation of methylcyclohexane and hydrogen production. Structural characterizations evidenced that the modification partially influenced the surface area, the pore structure, and the oxygen-containing functional groups of the supports. The techniques of CO pulse, transmission electron microscopy, and hydrogen temperature-programmed reduction were utilized to investigate the dispersion degrees and particle sizes of the active component Pt, and its interaction with the various functionalized supports, respectively. The results manifested that Pt particles loaded on the functionalized PTC-S had the largest dispersion degree and the smallest size among those loaded on PTC and other functionalized PTC (i.e., PTC-K and PTC-NH). Finally, the Pt-based catalysts were successfully applied in the dehydrogenation reaction of methylcyclohexane to yield hydrogen. The results revealed that the Pt catalyst over the functional PTC-S support exhibited a more excellent conversion of methylcyclohexane (84.3%) and a higher hydrogen evolution rate (991.5 mmol/g<sub>Pt</sub>/min) than the other resulting Pt-based catalysts.

**Keywords:** Pt-based catalysts; functional pyrolytic activated carbon; waste tires; hydrogen energy; methylcyclohexane

## 1. Introduction

As one of the energies with the highest potential, hydrogen energy has attracted widespread attention due to its cleanness, conversion efficiency, environmental friendliness, etc. [1–4]. Liquid organic hydride (LOH) has been deemed an alternative hydrogen energy carrier for the advantages that include high hydrogen storage capacity, high energy density, facile storage, convenient transportation in safe conditions (i.e., liquid), and a highly reversible hydrogenation–dehydrogenation process [5–9]. A variety of liquid organic hydrides have been developed with cyclohexane, methylcyclohexane (MCH), 1, 4-dimethylcyclohexane, decalin, and so on. Among them, MCH is the most promising LOH for its high reversibility, favorable theoretical hydrogen-storage capacity (6.2 wt%), and low toxic dehydrogenation product (i.e., toluene) with respect to benzene [10]. The dehydrogenation of MCH can be accelerated in the presence of catalysts with the active components (e.g., Pt and Pd) over appropriate supports. Pt-based catalysts exhibited higher activity and better selectivity than Pd-based catalysts in the dehydrogenation reaction of

MCH [11–13]. A suitable support could be beneficial to improving the activity and stability of the Pt-based catalysts. Carbon materials have been considered to be desirable catalytic supports with the ability to promote the dispersion of platinum atoms because of their high specific surface area, well-developed porosity, strong mechanical resistance, and abundant surface oxygen-containing groups [14,15].

With the development of the automobile industry, millions of tires are discarded, thrown away, or buried all over the world annually. Meanwhile, the accumulation of waste tires has been sharply augmented by their low biodegradability, with their total reaching up to 5000 million by 2030 [16]. The growing number of waste tires will cause severe environmental pollution and threaten human health without being properly handled [17]. Compared to landfills and incineration, pyrolysis has been regarded as an efficient and eco-friendly handling approach for the high value-added recycled products. As one of the main pyrolytic products, pyrolytic carbon has shown a similar structure to carbon materials [18,19]. A significant number of researchers have discussed its utilizations for adsorbents [20–22], capacitor materials [23–25], catalyst supports [26–29], and so on. Furthermore, carbon supports could be improved in their surface area or functional groups to build blocks for the covalent attachment of transition-metal complexes [30]. Zhang's group reported an efficient support treated by sulfuric acid for the dehydrogenation of MCH [31]. Potassium hydroxide and aminopropyl triethoxysilane were utilized to modify the Al<sub>2</sub>O<sub>3</sub> or SBA-15 due to their high performance on the surface structures, the acidity and basicity of the supports, and the interaction with the active component, etc. [32–35].

Herein, we presented a serial of the functionalized pyrolytic activated carbon (PTC) derived from waste tires and investigated their performance on the dehydrogenation of MCH and hydrogen production. Characterizations suggested that the surface structures of PTC, including the surface area, the pore structure, and the oxygen-containing functional groups, were changed by the sulfuric acid (PTC-S), potassium hydroxide (PTC-K), and aminopropyl triethoxysilane (PTC-NH). The CO pulse technique and transmission electron microscopy (TEM) were used to investigate the dispersion degrees and the sizes of the Pt nanoparticles, and the hydrogen-temperature-programmed reduction (H<sub>2</sub>-TPR) technique was utilized to explore the interaction mechanism between the active component Pt and the various functionalized PTCs. Finally, the prepared Pt-based catalysts were successfully applied in the dehydrogenation reaction of MCH to produce hydrogen.

## 2. Experimental Section

### 2.1. Chemicals and Reagents

Pyrolytic carbon black derived from waste tires was purchased from Shanghai Greenman ECO Science and Technology Co., Ltd. (Shanghai, China). Chloroplatinic acid hydrate (99.95%) and ethylene glycol solution (99.5%) were purchased from Tianjin Jinhai Type Science and Technology Development Co., Ltd. (Tianjin, China) and Tianjin Jiangtian Chemical Technology Co., Ltd. (Tianjin, China), respectively. MCH (99.0%), toluene (99.5%), aminopropyl triethoxysilane (98.0%), potassium hydroxide (85.0%), and sulfuric acid (95.0%) were purchased from Tianjin Concord Technology Co., Ltd. (Tianjin, China). He (99.99%), 10% H<sub>2</sub>-90% Ar, and 10% CO-90% He gases were provided by the Beijing Green Oxygen Tiangang Technology Development Co., Ltd. (Beijing, China). Nitrogen gas was from Tianjin Sizhi Gas Co., Ltd. (Tianjin, China). Ultrapure water (18.2 MΩ·cm) was produced by a Milli-Q EQ 7000 (Merck Milipore, Shanghai, China) and utilized throughout the experiments.

### 2.2. Instruments

The scanning electron microscopy (SEM) and element mapping images were performed on a JEOL JSM-7500F (JEOL, Tokyo, Japan). TEM and high-resolution transmission electron microscopy (HRTEM) images were captured on a FEI Tecnai G<sup>2</sup> F20 (FEI, Eindhoven, Netherlands). The specific surface area and the pore structure of the carbon supports were obtained by a fully automatic multifunctional gas adsorption instrument ASAP 2020

(Micromeritics, Atlanta, GA, USA). A Vector 22 Fourier transform infrared (FTIR) spectrophotometer (Bruker, Switzerland) and a Kratos AXIS-ULTRA DLD multifunctional photoelectron spectrometer with Mg-K $\alpha$  radiation (Shimadzu, Kyoto, Japan) were utilized to measure the surface functional groups and the X-ray photoelectron spectroscopy data (XPS), respectively. All the XPS peaks were calibrated with the C1s peak binding energy of 284.5 eV for adventitious carbon. X-ray diffraction patterns (XRD) were recorded on a Bruker D8 FOCUS powder X-ray diffractometer (Bruker, Karlsruhe, Germany). A Renishaw inVia MicroRaman spectrometer (Renishaw, London, UK) was utilized to measure the Raman spectra with an excitation light of 514.5 nm. Load capacity of Pt was measured by an inductively coupled plasma atomic emission spectrometer (ICP-AES, ICP-9000(N+M), Shimadzu, Kyoto, Japan). A Thermo Plus EVO thermogravimetry-differential thermal analyzer (TG-DTA, Rigaku, Tokyo, Japan) was employed to measure TG and DTG curves with a heating rate of 10 °C/min in nitrogen. CO pulse and H<sub>2</sub>-TPR techniques were carried out on a Micromeritics Chemsorb 2750 equipped with a thermal conductivity detector (Micromeritics, Atlanta, GA, USA). The dehydrogenation reaction of MCH to yield hydrogen was performed on a fixed-bed flow reactor from Tianjin Pengxiang Technology Co., Ltd. (Tianjin, China). A Gas Chromatograph (GC)-7800 (Labthink, Jinan, China) equipped with a flame ionization detector and an SE-30 column was used to analyze the products of MCH dehydrogenation. All measurements were taken at room temperature.

### 2.3. Preparation of the PTC

20 g of the pyrolysis carbon black derived from waste tires was extracted in 300 mL of the toluene solution for 96 h to remove the organic impurities, subsequently acid-washed by 100 mL 0.1 mol·L<sup>-1</sup> of the dilute sulfuric acid at 40 °C for 12 h to eliminate the inorganic ash, and dried in an oven at 55 °C for 12 h. Finally, the purified carbon black was activated with steam at 850 °C for 2 h in a tube furnace to develop its porous system to prepare the PTC.

### 2.4. Preparation of the Functionalized PTC Supports

10 g of PTC was functionalized by 100 mL 2 mol/L of dilute sulfuric acid at 65 °C for 8 h, cooled naturally, washed, filtered, dried in an oven at 110 °C for 12 h, and marked as PTC-S. PTC-NH and PTC-K supports were prepared using the operations identical to PTC-S, but functionalized by aminopropyl triethoxysilane and potassium hydroxide, respectively.

### 2.5. Preparation of the Pt-Based Catalysts

Pt was loaded on the surface of the functionalized PTC supports to yield the Pt-based catalysts, which were prepared with the impregnation method as follows: 2.0 g PTC was dispersed into 20 mL ultrapure water and stirred for 20 min. 0.6 mL 6.98 mg·mL<sup>-1</sup> of chloroplatinic acid was added dropwise into the suspension and stirred for another 30 min. Then, 20 mL of ethylene glycol solution was added to pre-reduce the Pt-based precursor at 100 °C for 4 h. Finally, the stock solution cooled to room temperature, filtered, and collected the solid product (i.e., the Pt/PTC catalyst), which was washed with ultrapure water and dried in a vacuum at 55 °C for 12 h for further characterizations and applications. The loaded amount of Pt in the catalysts was around 0.2 wt%, which was measured by ICP-AES. The Pt/PTC-S, Pt/PTC-K, and Pt/PTC-NH catalysts were prepared by the same operations as the Pt/PTC catalyst, applying PTC-S, PTC-K, and PTC-NH as the supports, respectively.

### 2.6. Catalytic Reaction

Dehydrogenation reaction of MCH to produce hydrogen and toluene was performed in a fixed-bed flow reactor (10 mm inner diameter (ID) × 250 mm). Briefly, 0.03 mL/min of MCH was continuously injected into the reactor under a nitrogen stream. The reaction occurred at 300 °C for 12 h under 0.3 g of the Pt-based catalyst, which was freshly reduced with H<sub>2</sub> at 400 °C for 2 h. The products of catalytic reaction were separated by a gas-liquid separator under condensation conditions, which collected the liquid every hour.

The conversions of MCH were measured by a GC instrument. Each catalytic reaction was performed three times in parallel.

### 2.7. Recycling Assays

The heterogeneity and stability of the Pt-based catalyst were investigated by recycling assays. After the first run of the catalytic reaction finished, the catalyst was recovered, reduced with H<sub>2</sub> at 400 °C for 2 h, and reused for the next run's catalytic reaction. And it was implemented in another three runs. At the same time, the amounts of Pt in the recovered Pt-base catalyst and the filtrate were detected by ICP-AES after the first run.

## 3. Results and Discussion

### 3.1. Characterizations of the Functional PTC Supports

SEM (Figure 1A) showed that PTC was composed of a large number of regular spherical particles and various pores, both in favor of the loading of active components. As presented in the XRD patterns (Figure 1B), the diffraction peaks at 24° and 44° in PTC XRD originated from the (110) and (002) crystal faces of graphite microcrystalline (PDF# 041-1487), respectively. The same diffraction peaks were observed in PTC-S, PTC-K, and PTC-NK, which indicated that the crystal structure of the supports was little changed after being treated by dilute sulfuric acid, potassium hydroxide, and aminopropyl triethoxysilane. All the N<sub>2</sub> adsorption isotherms of the functional PTC supports (Figure 1C) were found in the H4 hysteresis loops, which indicated the presence of the mesopores [36]. The distribution of pore diameter (Figure 1D) verified that the presented supports exhibited an abundant pore structure, including a great number of micropores (0.45–0.7 nm, 1–2 nm) and a small number of mesopores (2–4 nm), which was the same result as N<sub>2</sub> adsorption isotherms. Compared to PTC, the pores of PTC-S appeared to slightly move to lower aperture. Moreover, the intensity of the 0.4–0.5 nm pores significantly decreased, which might have resulted from the sulfuric acid molecules entering into the pore structure and blocking the partial pores. Meanwhile, the porous distribution of PTC-K appeared the addition of the 0.3–0.4 nm micropore in comparison to PTC, which indicated that the potassium hydroxide had a little influence on the pore structure. Whereas the pore structures of PTC-NH were extremely changed, which might be attributed to the blockage of small pores (less than 0.5 nm) and the addition of the 0.7–3 nm pores, suggesting that the surface structures of PTC were affected by aminopropyl triethoxysilane. Table 1 lists the specific surface areas and the pore structures of the PTC, PTC-S, PTC-K, and PTC-NH supports. The specific surface area, pore volume, and pore size of PTC were 902 m<sup>2</sup>/g, 1.071 cm<sup>3</sup>/g, and 4.75 nm, respectively, which were slightly changed in those of PTC-S and PTC-K. Nevertheless, the surface area and pore volume of PTC-NH decreased to 490 m<sup>2</sup>/g and 0.833 cm<sup>3</sup>/g, respectively, while the pore size increased to 6.80 nm, which resulted from the blockage of small pores and the expansion of partial pores during the treatment [37].

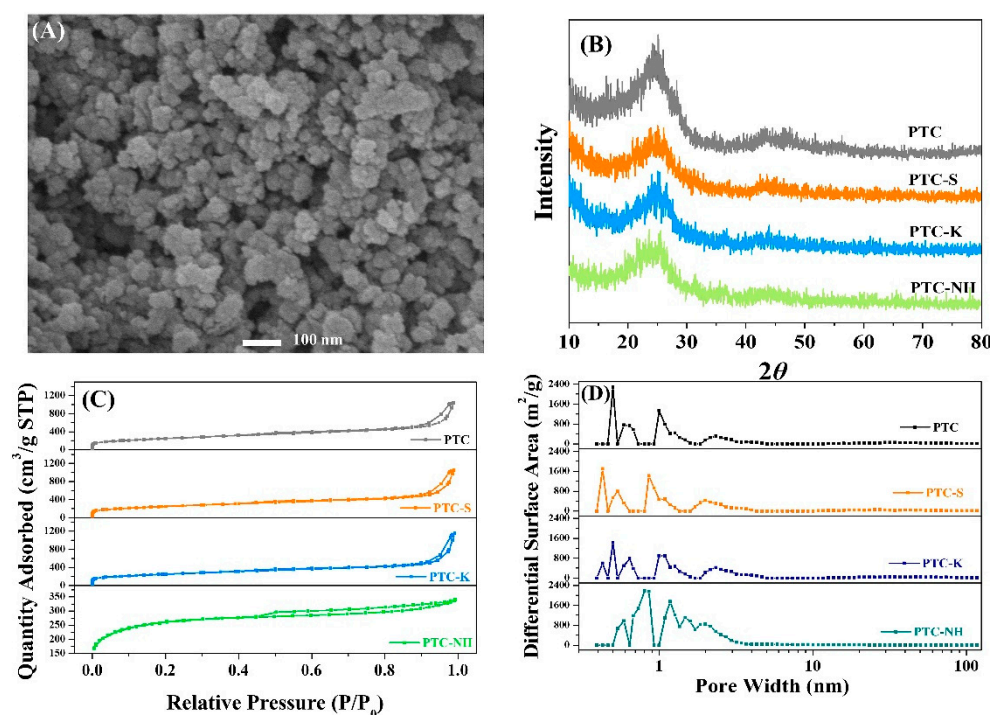


**Figure 1.** (A) SEM of PTC, (B) XRD patterns, (C) N<sub>2</sub> adsorption isotherms, and (D) pore size distributions of the PTC, PTC-S, PTC-K, and PTC-NH supports.

**Table 1.** The surface structural properties of the PTC, PTC-S, PTC-K, and PTC-NH supports.

Supports	Surface Area (m <sup>2</sup> /g)	Pore Volume (cm <sup>3</sup> /g)	Pore Size (nm)
PTC	902	1.071	4.75
PTC-S	898	1.133	5.05
PTC-K	906	1.160	5.12
PTC-NH	490	0.833	6.80

The structural properties of PTC and PTC-S were further analyzed by the characterizations of Raman, FTIR, DG, DTG, and XPS techniques. As revealed in Figure 2A, both D-band peaks (1345 cm<sup>-1</sup>, 1342 cm<sup>-1</sup>) and G-band peaks (1589 cm<sup>-1</sup>, 1600 cm<sup>-1</sup>) were observed in the Raman spectra of PTC and PTC-S, respectively, which indicated the presence of the amorphous carbon (sp<sup>3</sup>) and the crystal carbon (sp<sup>2</sup>) in PTC and PTC-S [38]. The result was consistent with that of XRD patterns. The proportion of D-band peak intensity (I<sub>D</sub>) to G-band peak intensity (I<sub>G</sub>) expressed the disorder degree of carbon materials [39]. I<sub>D</sub>/I<sub>G</sub> was 0.909 for PTC and 1.01 for PTC-S, which displayed the increase in the disorder degree after the treatment by dilute sulfuric acid. The probable reason was that the sp<sup>2</sup> type carbon (C=C) was partly oxidized to the sp<sup>3</sup> type carbon (C-C/C-S) by dilute sulfuric acid. This phenomenon was similar to that of the reported literature [40]. Moreover, the intensities of the 2D-band peak (2677 cm<sup>-1</sup>) and 2G-band peak (2928 cm<sup>-1</sup>) in the Raman spectrum of PTC-S were obviously enhanced in comparison to those in the PTC Raman spectrum. The FTIR spectrum (Figure 2B) evidenced the abundant oxygen-containing functional groups on the surface of PTC and PTC-S. The absorption peaks at 3450 cm<sup>-1</sup> and 1630 cm<sup>-1</sup> were attributed to the stretching vibration of the O-H bond [41] and the C=O bond [42], respectively. The peaks *ca.* 1100 cm<sup>-1</sup> and 540 cm<sup>-1</sup> were assigned to the stretching vibration of the C-O bond [43] and C-S bond [44,45]. Compared to PTC, the new absorption peak at 620 cm<sup>-1</sup> was ascribed to the stretching vibration of the S=O bond in the sulfuric acid group [46], which further indicated that the surface functional groups of PTC were modified by sulfuric acid. As displayed in Figure 2C of the PTC TG and DTG profiles, the peaks at 250 °C and 460 °C were ascribed to the decomposition of the carboxyl group

and carboxyl anhydrides [47]. The peak at 156 °C in the TG and DTG curves of PTC-S (Figure 2D) was attributed to the loss of moisture, and those at 248 °C and 400 °C were assigned to the decomposition of the carboxyl group and carboxyl anhydrides/sulfuric acid groups, respectively [48,49].

XPS further evidenced the surface structure of PTC and PTC-S. As observed in Figure 2E, the surface of PTC was composed of C, O, and S elements. In the C 1s spectrum of PTC (Figure 2F), the XPS peaks were located at 284.5, 286.0, 288.8, and 290.9 eV, which were assigned to C-C, C-O-C, O-C=O, and C-S bonds, respectively [50,51]. The O 1s spectrum (Figure 2G) was constituted by the peaks of 532.2, 533.5, and 535.6 eV, indicating the presence of C=O and C-O bonds. The S element in PTC was probably produced from the vulcanization process of the tire. The doublet peak of the S 2p spectrum (Figure 2H) resulted from the spin-orbit coupling of the S 2p<sub>3/2</sub> (163.9 eV) and S 2p<sub>1/2</sub> components (165.1 eV) [40]. The wide spectrum of PTC-S (Figure 2I) revealed that PTC-S contained the C, O, and S elements, which was similar to that of PTC. However, the level of the S element increased relative to that in PTC, which resulted from the successful functionalization by the dilute sulfuric acid. Meanwhile, the C-C bond (284.5 eV), C-O-C bond (286.1 eV), O-C=O bond (288.4 eV), and C-S bond (291.0 eV) were observed in the C 1s spectrum of PTC-S (Figure 2J). Compared to the O 1s spectrum of PTC, the new peak located at 535.7 eV in the O 1s spectrum (Figure 2K) was originated by the S-O bond. Likewise, the S 2p spectrum of PTC-S (Figure 2L) was found another peak at 169 eV in contrast with that of PTC, which was ascribed to the sulfate species [52], convincingly demonstrating the introduction of the sulfuric acid group. The doublet split into the S 2p<sub>3/2</sub> (168.2 eV) and S 2p<sub>1/2</sub> (169.4 eV) components [53]. The results of the XPS files were consistent with that of FTIR.

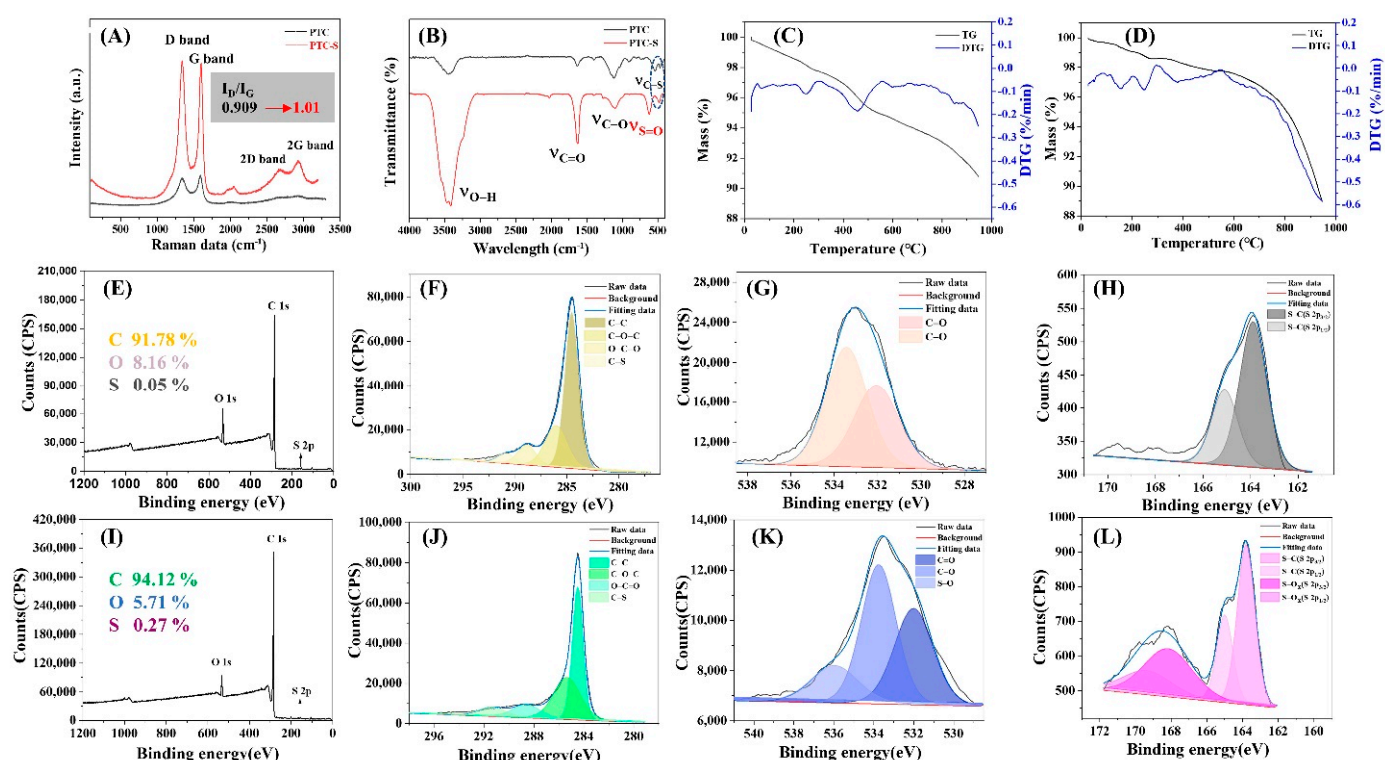


**Figure 2.** (A) Raman spectra and (B) FTIR spectra of PTC and PTC-S; (C) TG and DTG curves of PTC; (D) TG and DTG curves of PTC-S; (E) Survey, (F) C 1s, (G) O 1s, (H) S 2p spectra of PTC; (I) Survey, (J) C 1s, (K) O 1s, (L) S 2p spectra of PTC-S.

### 3.2. Characterizations of the Pt-Based Catalysts over the Functional PTC Supports

As shown in the XRD patterns (Figure 3A), the diffraction peaks of Pt were not found in the Pt-based catalysts, which indicated the effective dispersion of Pt particles on the

functionalized PTC supports. H<sub>2</sub>-TPR curves (Figure 3B) evidenced the reduced mechanism of the Pt-based catalysts by H<sub>2</sub>. The peak at 605 °C was observed in the H<sub>2</sub>-TPR curve of PTC, which originated from the surface intrinsic functional groups of carbon materials. In comparison with PTC, the H<sub>2</sub>-TPR curve of the Pt/PTC catalyst exhibited a wide weak peak at 246 °C, which was generated by the reduction reaction of Pt-O-Pt or Pt-O-C [54], demonstrating the successful loading of the active component Pt. Likewise, the distinct or weak peaks of Pt-O-C or Pt-O-Pt were discovered in the H<sub>2</sub>-TPR curves of Pt/PTC-S, Pt/PTC-K, and Pt/PTC-NH, which manifested the successful preparation of Pt/PTC-S, Pt/PTC-K, and Pt/PTC-NH. Additionally, the locations of the reduction peaks were less than 400 °C, which suggested that the active component Pt could be reduced into the metallic state by H<sub>2</sub> at 400 °C.

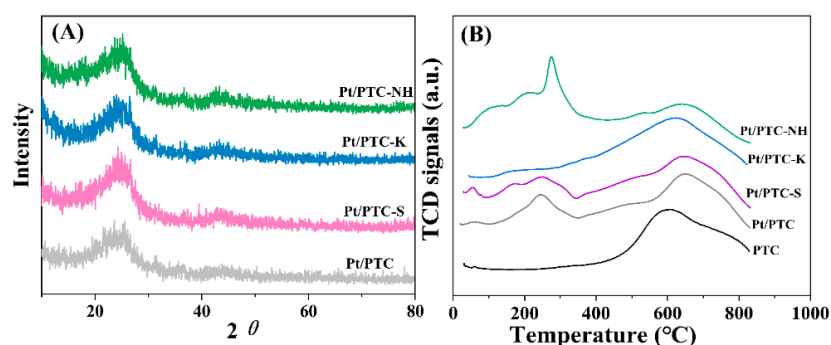


**Figure 3.** (A) XRD patterns and (B) H<sub>2</sub>-TPR curves of the Pt catalysts over the functional PTC supports.

Figure 4 depicts the TEM and HRTEM images of Pt/PTC and Pt/PTC-S. As shown in Figure 4A, the average size of the Pt particles in the Pt/PTC catalyst was *ca.* 4.2 nm. As exhibited in Figure 4B, the Pt particles in the Pt/PTC-S catalyst appeared well dispersed, with an average size of 2.1 nm. Noticeably, the PTC-S support had a small number of the 2~4 nm pores (pore size distribution in Figure 1D), which resulted in the Pt particles that entered into these pores hardly enlarging any further due to the limitation in pore size and the strong interaction between Pt and the pre-introduced sulfur. The insets in Figure 4A,B illustrate that the lattice spaces of Pt in the Pt/PTC and Pt/PTC-S catalysts were 0.22 and 0.23 nm, respectively, which were attributed to the Pt (111) crystal face and were a benefit to the dehydrogenation of MCH [55]. The elemental mapping images confirmed the existence of C, O, S, and Pt, which further indicated the effective dispersion of Pt particles in the Pt/PTC-S catalyst.

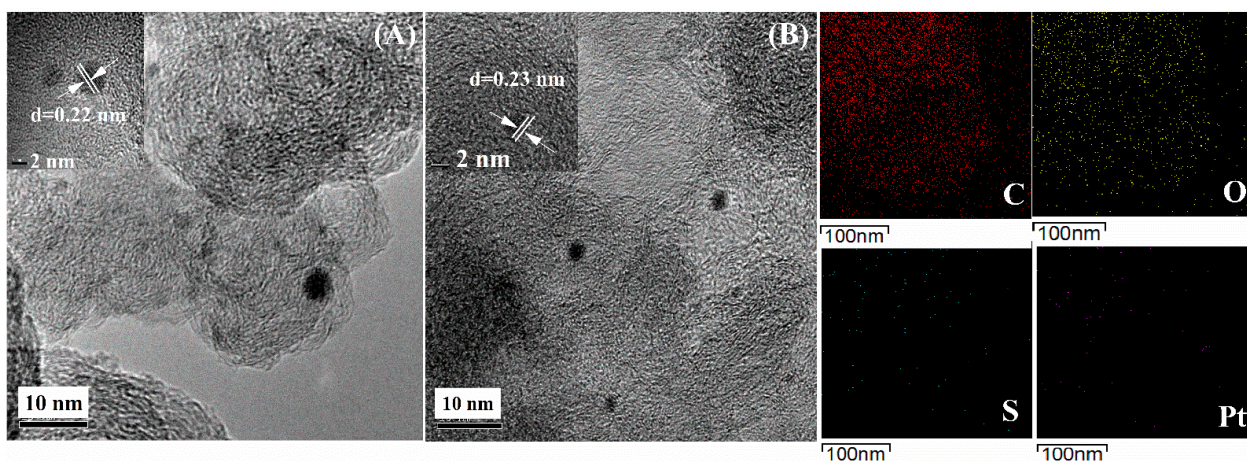


**Figure 4.** (A) TEM and HRTEM images of Pt/PTC; (B) TEM and HRTEM images of Pt/PTC-S, the element mapping images of C, O, S, and Pt in Pt/PTC-S.

The dispersion degrees of the active component Pt particles over the supports significantly affect the catalytic activity, which were measured by the CO pulse adsorption technique. As listed in Table 2, the dispersion degree of Pt particles in Pt/PTC was 25.6%, which was improved extremely to 53.4% in Pt/PTC-S, resulting from the strong affinity between platinum atoms and sulfur on the functionalized PTC-S that prevented Pt atom diffusion and enhanced its dispersion [56–58]. The sizes of Pt particles in Pt/PTC and Pt/PTC-S were 4.42 nm and 2.12 nm, respectively, which was in agreement with that of TEM. However, the dispersion degrees of the active component Pt in the Pt/PTC-K and Pt/PTC-NH catalysts were 12.2% with a size of 9.31 nm, and 4.3% with a size of 26.3 nm, respectively, which confirmed that the Pt particles suffered from agglomeration on the functionalized PTC-K and PTC-NH supports.

**Table 2.** The dispersion degrees of active component Pt particles in the Pt-loaded catalysts.

Catalysts	Adsorption Capacity of CO ( $\mu\text{L/g}$ Catalysts)	Surface Area of Metal ( $\text{m}^2/\text{g}$ Sample)	Dispersion of Active Component Pt (%)	Mean Size of Pt (nm)
Pt/PTC	58.9	63.3	25.6	4.42
Pt/PTC-S	122.7	131.9	53.4	2.12
Pt/PTC-K	28.0	30.1	12.2	9.31
Pt/PTC-NH	9.89	10.6	4.3	26.3

### 3.3. Optimization of Dehydrogenation Reaction Conditions

It was investigated that the influences of reaction temperature and weight hourly space velocity (WHSV) on the conversion of MCH and the hydrogen evolution rate. As shown in Figure 5A, the conversions of MCH to produce hydrogen utilizing Pt/PTC-S as a catalyst were 7.11%, 33.7%, and 83.5% when setting the reaction temperature at 260 °C, 280 °C, and 300 °C, respectively, owing to the endothermic reaction of the MCH dehydrogenation reaction. However, the conversion of MCH at 320 °C was 83.7%, which was identical to that at 300 °C, indicating that the optimum reaction temperature was 300 °C. Meanwhile, as WHSV increased, the conversion of MCH significantly decreased, but the change in the hydrogen evolution rate was not evident (Figure 5B). In order to save cost,  $4.74 \text{ h}^{-1}$  (i.e., 0.30 mL/min of MCH) of WHSV was employed in the dehydrogenation reaction of MCH.

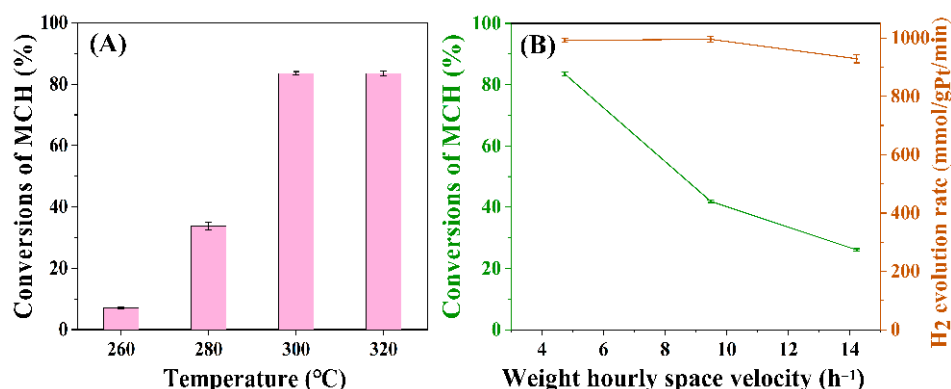


**Figure 5.** (A) The influence of reaction temperature on the conversion of MCH using Pt/PTC-S as the catalyst; (B) the effect of weight hourly space velocity (WHSV) on the conversion of MCH and the hydrogen evolution rate under the Pt/PTC-S catalyst.

### 3.4. Dehydrogenation of MCH by the Pt-Based Catalysts over the Functional PTC Supports

Figure 6 exhibits the conversions of MCH and the hydrogen evolution rates taking Pt/PTC, Pt/PTC-S, Pt/PTC-K, and Pt/PTC-NH as catalysts at 300 °C. As shown in Figure 6A, the conversion of MCH using Pt/PTC as the catalyst was 40.1% at 2 h, but slightly decreased from 41.5 to 38.2%, with the reaction time increasing from 3 to 12 h. Moreover, the conversion of MCH adopting Pt/PTC-S as the catalyst was firstly around

76.4% at 2 h and kept stable at 84.3% as the reaction time increased from 3 to 12 h, which was distinctly higher and more stable than that of Pt/PTC, originating from the strong and thermally stable Pt-S bonding [59]. However, the conversions of MCH utilizing Pt/PTC-K and Pt/PTC-NH as catalysts were nearly 0, which probably resulted from the low dispersion degrees and the large sizes of the active component Pt in two catalysts, indicating that potassium hydroxide and aminopropyl triethoxysilane were not suitable as the modification agents of PTC for the catalytic dehydrogenation of MCH. The hydrogen evolution rate of Pt/PTC was 453.4 mmol/g<sub>Pt</sub>/min, which increased up to 991.5 mmol/g<sub>Pt</sub>/min in Pt/PTC-S, further indicating the good catalytic activity of Pt/PTC-S (Figure 6B). Figure 6C demonstrates the recycling study of the Pt/PTC-S catalyst. The conversions of MCH in the four reuses of Pt/PTC-S were revealed to fluctuate a little in the range of 82.1~84.0%, which indicated the high stability of the Pt/PTC-S catalyst. Pt leaching in the reaction was 0.14 ppm after the first run. Additionally, when the Pt catalyst was filtrated from the reaction system, the catalytic reaction was rarely measured by the filtrate, which proved that Pt on carbon supports was the heterogeneous active site. Table 3 lists the comparisons of the hydrogen production of Pt-based catalysts over other supports reported by the previous literature, which manifested the high performance of the resultant Pt/PTC-S for hydrogen production.

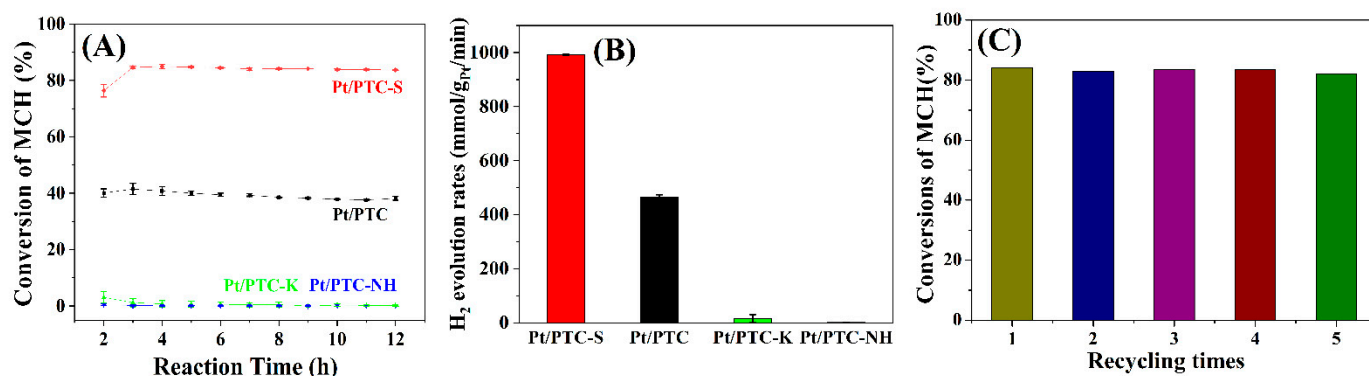


**Figure 6.** (A) The conversions of MCH dehydrogenated into toluene by Pt-based catalysts; (B) the hydrogen evolution rates of the Pt-based catalysts; (C) recycling study of Pt/PTC-S.

**Table 3.** Comparison of dehydrogenation of MCH and hydrogen production with other Pt catalysts reported in the literature at 300 °C.

Catalysts	Temperature (°C)	Rate of Liquid MCH (mL/min)	Catalyst Weight	Pt loading Content (wt %)	Conversion of MCH (%)	H <sub>2</sub> Evolution Rate (mmol/g <sub>Pt</sub> /min)	Refs.
Pt/SBA-15	300 °C	0.03	0.05	3	65 (initial)	308.6	[60]
Pt/Ce-Mg-Al O	300 °C	-	-	0.35	49.8	686.9	[61]
Pt/coconut activated carbon	300 °C	0.03	0.03	1	42	598.2	[62]
Pt/pyrolytic waste activated carbon	300 °C	0.03	0.554	0.4	95	305.3	[29]
Pt/GAC-S	300 °C	0.03	0.3	0.2	63	741.1	[31]
PtSn-5/Mg-Al-O-350	300 °C	0.1	0.5	2	90.5	214.8	[63]
Pt/PTC-S	300 °C	0.03	0.3	0.2	84.3	991.5	This work

#### 4. Conclusions

Herein, we presented a high-performance support for hydrogen production based on the functionalized pyrolytic activated carbon derived from waste tires. N<sub>2</sub>-adsorption, FTIR, CO pulse, and XPS suggested that the modification by sulfuric acid, potassium hydroxide, and aminopropyl triethoxysilane influenced the surface area, the pore structure, and the oxygen-containing functional groups of the supports, thereby affecting the Pt particles in Pt-based catalysts in terms of particle size, dispersion, and dehydrogenation activity. Results indicated that the sulfuric acid group exhibited the ability to promote the dispersion of the active component Pt over the support and enhance the stability of the Pt/PTC-S catalyst. Furthermore, satisfactory enhancements were observed in the MCH conversion (84.3%) and hydrogen production (991.5 mmol/g<sub>Pt</sub>/min) of the catalyst over the sulfonic-function PTC with respect to other functional PTC at 300 °C.

**Author Contributions:** Conceptualization, H.Y. and C.Z.; methodology, H.Y., T.W. and C.Z.; formal analysis, H.Y.; investigation, H.Y.; resources, Y.C.; data curation, C.Z.; writing—original draft preparation, H.Y.; writing—review and editing, C.Z. and Y.C.; visualization, S.L.; supervision, S.L.; project administration, C.Z.; funding acquisition, C.Z. and Y.C. All authors have read and agreed to the published version of the manuscript.

**Funding:** This research was funded by the National Natural Science Foundation of China and Key Project of Tianjin Application Foundation and Frontier Plan, grant numbers 21003077 and 14JCZDJC32000.

**Institutional Review Board Statement:** Not applicable.

**Informed Consent Statement:** Not applicable.

**Data Availability Statement:** Data sharing is not applicable.

**Acknowledgments:** This work was supported by the National Natural Science Foundation of China (no.: 21003077) and Key Project of Tianjin Application Foundation and Frontier Plan (no.: 14JCZDJC32000).

**Conflicts of Interest:** The authors declare no conflict of interest.

**Sample Availability:** Samples are not available from the authors.

#### References

1. Lee, H.; Kim, A.; Lee, B.; Lim, H. Comparative numerical analysis for an efficient hydrogen production via a steam methane reforming with a packed-bed reactor, a membrane reactor, and a sorption-enhanced membrane reactor. *Energy Convers. Manag.* **2020**, *213*, 112839. [[CrossRef](#)]
2. Burhan, M.; Shahzad, M.W.; Oh, S.J.; Ng, K.C. A pathway for sustainable conversion of sunlight to hydrogen using proposed compact CPV system. *Energy Convers. Manag.* **2018**, *165*, 102–112. [[CrossRef](#)]
3. Li, Z.; Yao, Z.H.; Haidry, A.A.; Plecenik, T.; Grancic, B.; Roch, T.; Gregor, M.; Plecenik, A. The effect of Nb doping on hydrogen gas sensing properties of capacitor-like Pt/Nb-TiO<sub>2</sub>/Pt hydrogen gas sensors. *J. Alloys Compd.* **2019**, *806*, 1052–1059. [[CrossRef](#)]
4. Mohammadi, A.; Mehrpooya, M. Techno-economic analysis of hydrogen production by solid oxide electrolyzer coupled with dish collector. *Energy Convers. Manag.* **2018**, *173*, 167–178. [[CrossRef](#)]
5. Salkuyeh, Y.K.; Saville, B.A.; MacLean, H.L. Techno-economic analysis and life cycle assessment of hydrogen production from natural gas using current and emerging technologies. *Int. J. Hydrogen Energy* **2017**, *42*, 18894–18909. [[CrossRef](#)]
6. Zhu, Q.L.; Xu, Q. Liquid organic and inorganic chemical hydrides for high-capacity hydrogen storage. *Energy Environ. Sci.* **2015**, *8*, 478–512. [[CrossRef](#)]
7. Kariya, N.; Fukuoka, A.; Ichikawa, M. Efficient evolution of hydrogen from liquid cycloalkanes over Pt-containing catalysts supported on active carbons under “wet–dry multiphase conditions”. *Appl. Catal. A* **2002**, *233*, 91–102. [[CrossRef](#)]
8. Kou, Z.; Zhi, Z.; Xu, G.; An, Y.; He, C. Investigation of the performance and deactivation behavior of Raney-Ni catalyst in continuous dehydrogenation of cyclohexane under multiphase reaction conditions. *Appl. Catal. A* **2013**, *467*, 196–201. [[CrossRef](#)]
9. Li, J.F.; Chai, Y.M.; Liu, B.; Wu, Y.L.; Li, X.H.; Tang, Z.; Liu, Y.Q.; Liu, C.G. The catalytic performance of Ni<sub>2</sub>P/Al<sub>2</sub>O<sub>3</sub> catalyst in comparison with Ni/Al<sub>2</sub>O<sub>3</sub> catalyst in dehydrogenation of cyclohexane. *Appl. Catal. A* **2014**, *469*, 434–441. [[CrossRef](#)]
10. Zahid, A.H.; Amin, N.; Nisar, F.; Saghir, S. Analysis of MTH-System (Methylcyclohexane-Toluene-Hydrogen-System) for hydrogen production as fuel for power plants. *Int. J. Hydrogen Energy* **2020**, *45*, 32234–32242. [[CrossRef](#)]
11. Shukla, A.A.; Gosavi, P.V.; Pande, J.V.; Kumar, V.P.; Chary, K.V.R.; Biniwale, R.B. Efficient hydrogen supply through catalytic dehydrogenation of methylcyclohexane over Pt/metal oxide catalysts. *Int. J. Hydrogen Energy* **2010**, *35*, 4020–4026. [[CrossRef](#)]
12. Miao, L.; Yan, J.; Wang, W.Y.; Huang, Y.P.; Li, W.S.; Yang, Y.Q. Dehydrogenation of methylcyclohexane over Pt supported on Mg-Al mixed oxides catalyst: The effect of promoter Ir. *Chin. J. Chem. Eng.* **2020**, *28*, 2337–2342. [[CrossRef](#)]

13. Sugiura, Y.; Nagatsuka, T.; Kubo, K.; Hirano, Y.; Nakamura, A.; Miyazawa, K.; Iizuka, Y.; Furuta, S.; Iki, H.; Higo, T.; et al. Dehydrogenation of Methylcyclohexane over Pt/TiO<sub>2</sub>-Al<sub>2</sub>O<sub>3</sub> Catalysts. *Chem. Lett.* **2017**, *46*, 1601–1604. [[CrossRef](#)]
14. Jiang, Z.; Guo, S.; Fang, T. Enhancing the catalytic activity and selectivity of PdAu/SiO<sub>2</sub> bimetallic catalysts for dodecahydro-N-ethylcarbazole dehydrogenation by controlling the particle size and dispersion. *ACS Appl. Energy Mater.* **2019**, *2*, 7233–7243. [[CrossRef](#)]
15. Copéret, C.; Adolfsson, H.; Sharpless, K.B. A simple and efficient method for epoxidation of terminal alkenes. *Chem. Commun.* **1997**, *16*, 1565–1566. [[CrossRef](#)]
16. Thomas, B.S.; Gupta, R.C.; Panicker, V.J. Recycling of waste tire rubber as aggregate in concrete: Durability-related performance. *J. Clean. Prod.* **2016**, *112*, 504–513. [[CrossRef](#)]
17. Brandsma, S.H.; Brits, M.; Groenewoud, Q.R.; Velzen, M.J.M.; Leonards, P.E.G.; Boert, J. Chlorinated Paraffins in Car tires recycled to rubber granulates and play-ground tiles. *Environ. Sci. Technol.* **2019**, *53*, 7595–7603. [[CrossRef](#)]
18. Darmstadt, H.; Roy, C.; Kaliaguine, S. ESCA characterization of commercial carbon blacks and carbon blacks from vacuum pyrolysis of used tires. *Carbon* **1994**, *32*, 1399–1405. [[CrossRef](#)]
19. Lee, W.H.; Kim, J.Y.; Ko, Y.K.; Reucroft, P.J.; Zondlo, J.W. Surface analysis of carbon black waste materials from tire residues. *Appl. Surf. Sci.* **1999**, *141*, 107–113. [[CrossRef](#)]
20. Makrigianni, V.; Giannakas, A.; Deligiannakis, Y.; Konstantinou, I. Adsorption of phenol and methylene blue from aqueous solutions by pyrolytic tire char: Equilibrium and kinetic studies. *J. Environ. Chem. Eng.* **2015**, *3*, 574–582. [[CrossRef](#)]
21. Salehs, T.A.; Al-Saadi, A.A.; Gupta, V.K. Carbonaceous adsorbent prepared from waste tires: Experimental and computational evaluations of organic dye methyl orange. *J. Mol. Liq.* **2014**, *191*, 85–91. [[CrossRef](#)]
22. Esfandbod, M.; Merritt, C.R.; Rashti, M.R.; Singh, B.; Boyd, S.E.; Srivastava, P.; Brown, C.L.; Butler, O.M.; Kookana, R.S.; Chen, C. Role of oxygen-containing functional groups in forest fire-generated and pyrolytic chars for immobilization of copper and nickel. *Environ. Pollut.* **2017**, *220*, 946–954. [[CrossRef](#)]
23. Han, Y.; Dong, X.T.; Zhang, C.; Liu, S.X. Hierarchical porous carbon hollow-spheres as a high performance electrical double-layer capacitor material. *J. Power Sources* **2012**, *211*, 92–96. [[CrossRef](#)]
24. Han, Y.; Dong, X.T.; Zhang, C.; Liu, S.X. Easy synthesis of honeycomb hierarchical porous carbon and its capacitive performance. *J. Power Sources* **2013**, *227*, 118–122. [[CrossRef](#)]
25. Han, Y.; Zhao, P.P.; Dong, X.T.; Zhang, C.; Liu, S.X. Improvement in electrochemical capacitance of activated carbon from scrap tires by nitric acid treatment. *Front. Mater. Sci.* **2014**, *8*, 391–398. [[CrossRef](#)]
26. Ji, R.N.; Yu, K.; Lou, L.L.; Zhang, C.; Han, Y.; Pan, S.; Liu, S.X. Chiral Mn (III) salen complexes immobilized directly on pyrolytic waste tire char for asymmetric epoxidation of unfunctionalized olefins. *Inorg. Chem. Commun.* **2012**, *25*, 65–69. [[CrossRef](#)]
27. Simaioforidou, A.; Papastergiou, M.; Margellou, A.; Petrakis, D.; Louloudi, M. Activated vs. pyrolytic carbon as support matrix for chemical functionalization: Efficient heterogeneous non-Heme Mn (II) catalysts for alkene oxidation with H<sub>2</sub>O<sub>2</sub>. *J. Mol. Catal. A Chem.* **2017**, *426*, 516–525. [[CrossRef](#)]
28. Seristatidou, E.; Mavrogiorgou, A.; Konstantinou, I.; Louloudi, M.; Deligiannakis, Y. Recycled carbon (RC) materials made functional: An efficient heterogeneous Mn-RC catalyst. *J. Mol. Catal. A Chem.* **2015**, *403*, 84–92. [[CrossRef](#)]
29. Zhang, C.; Liang, X.Q.; Liu, S.X. Hydrogen production by catalytic dehydrogenation of methylcyclohexane over Pt catalysts supported on pyrolytic waste tire char. *Int. J. Hydrogen Energy* **2011**, *36*, 8902–8907. [[CrossRef](#)]
30. Mavrogiorgou, A.; Simaioforidou, A.; Louloudi, M. Pyrolytic carbon as support matrix for heterogeneous oxidation catalysts: The influence of pyrolytic process on catalytic behavior. *J. Environ. Chem. Eng.* **2018**, *6*, 1127–1136. [[CrossRef](#)]
31. Ye, H.L.; Liu, S.X.; Zhang, C.; Cai, Y.Q.; Shi, Y.F. Dehydrogenation of methylcyclohexane over Pt-based catalysts supported on functional granular activated carbon. *RSC Adv.* **2021**, *11*, 29287–29297. [[CrossRef](#)]
32. Cansado, I.P.P.; RamiroBelo, C.; Mourão, P.A. Pesticides abatement using activated carbon produced from a mixture of synthetic polymers by chemical activation with KOH and K<sub>2</sub>CO<sub>3</sub>. *Environ. Nanotechnol. Monit. Manag.* **2019**, *12*, 100261. [[CrossRef](#)]
33. Li, W.Q.; Wang, F.M.; Zhan, X.B.; Sun, M.S.; Hu, J.Q.; Zhai, Y.; Lv, H.H.; Lv, G.J. Highly dispersed Pd nanoparticles supported on  $\gamma$ -Al<sub>2</sub>O<sub>3</sub> modified by minimal 3-aminopropyltriethoxysilane as effective catalysts for 2-ethyl-anthraquinone hydrogenation. *Appl. Catal. A* **2021**, *619*, 118124. [[CrossRef](#)]
34. Feng, J.T.; Wang, H.Y.; Evans, D.G.; Duan, X.; Li, D.Q. Catalytic hydrogenation of ethylantraquinone over highly dispersed eggshell Pd/SiO<sub>2</sub>-Al<sub>2</sub>O<sub>3</sub> spherical catalysts. *Appl. Catal. A* **2010**, *382*, 240–245. [[CrossRef](#)]
35. Ma, Q.Q.; Wang, N.; Liu, G.Z.; Wang, L. Enhanced performance of Pd nanoparticles on SBA-15 grafted with alkyltrialkoxysilane in 2-ethyl-anthraquinone hydrogenation. *Microporous Mesoporous Mater.* **2019**, *279*, 245–251. [[CrossRef](#)]
36. Qi, B.; Wang, Y.B.; Lou, L.L.; Huang, L.Y.; Yang, Y.; Liu, S.X. Solvent-free aerobic oxidation of alcohols over palladium supported on MCM-41. *J. Mol. Catal. A Chem.* **2013**, *370*, 95–103. [[CrossRef](#)]
37. Iost, K.N.; Borisov, V.A.; Temerev, V.L.; Surovikin, Y.V.; Pavluchenko, P.E.; Trenikhin, M.V.; Arbuzov, A.B.; Shlyapin, D.A.; Tsyrlunikov, P.G.; Vedyagin, A.A. Mechanism of Pt interfacial interaction with carbonaceous support under reductive conditions. *React. Kinet. Mech. Catal.* **2019**, *127*, 103–115. [[CrossRef](#)]
38. Zhong, Y.L.; Sun, X.T.; Wang, S.Y.; Peng, F.; Bao, F.; Su, Y.Y.; Li, Y.Y.; Lee, S.T.; He, Y. Facile, large-quantity synthesis of stable, tunable-color silicon nanoparticles and their application for long-term cellular imaging. *ACS Nano* **2015**, *9*, 5958–5967. [[CrossRef](#)]

39. Zhu, S.; Wang, L.; Li, B.; Song, Y.; Zhao, X.; Zhang, G.; Zhang, S.; Lu, S.; Zhang, J.; Wang, H.; et al. Investigation of photoluminescence mechanism of graphene quantum dots and evaluation of their assembly into polymer dots. *Carbon* **2014**, *77*, 462–472. [[CrossRef](#)]
40. Hosseini, M.S.; Masteri-Farahani, M.; Shahsavarifar, S. Chemical modification of reduced graphene oxide with sulfonic acid groups: Efficient solid acids for acetalization and esterification reactions. *J. Taiwan Inst. Chem. Eng.* **2019**, *102*, 34–43. [[CrossRef](#)]
41. Pyanova, L.G.; Luzyanina, L.S.; Drozdov, V.A.; Veselovskaya, A.V.; Arbuzov, A.B.; Likhobolov, V.A. Study of the effect of a number of oxidizers on variation of composition of surface functional groups, porous structure, and adsorption properties of composite carbon-carbon sorbent. *Prot. Met. Phys. Chem. Surf.* **2010**, *46*, 320–324. [[CrossRef](#)]
42. Tang, X.D.; Yu, H.M.; Bui, B.; Wang, L.Y.; Xing, C.; Wang, S.Y.; Chen, M.L.; Hu, Z.Z.; Chen, W. Nitrogen-doped fluorescence carbon dots as multi-mechanism detection for iodide and curcumin in biological and food samples. *Bioact. Mater.* **2021**, *6*, 1541–1554. [[CrossRef](#)] [[PubMed](#)]
43. Sandt, C.; Waeytens, J.; Deniset-Besseau, A.; Nielsen-Leroux, C.; Réjasset, A. Use and misuse of FTIR spectroscopy for studying the bio-oxidation of plastics. *Spectrochim. Acta Part A* **2021**, *258*, 119841. [[CrossRef](#)] [[PubMed](#)]
44. Yu, Y.X.; Rowland, C.E.; Schaller, R.D.; Korgel, B.A. Synthesis and ligand exchange of thiol-capped silicon nanocrystals. *Langmuir* **2015**, *31*, 6886–6893. [[CrossRef](#)] [[PubMed](#)]
45. Baik, S.; Zhang, H.; Kim, Y.K.; Harbottle, D.; Lee, J.W. Enhanced adsorption capacity and selectivity towards strontium ions in aqueous systems by sulfonation of CO<sub>2</sub> derived porous carbon. *RSC Adv.* **2017**, *7*, 54546–545537. [[CrossRef](#)]
46. Yu, H.; Jin, Y.; Li, Z.; Peng, F.; Wang, H. Synthesis and characterization of sulfonated single-walled carbon nanotubes and their performance as solid acid catalyst. *J. Solid State Chem.* **2008**, *181*, 432–438. [[CrossRef](#)]
47. Machado, J.; Castanheiro, J.E.; Matos, I.; Ramos, A.M.; Vital, J.; Fonseca, I.M. SBA-15 with sulfonic acid groups as a Green Catalyst for the acetoxylation of  $\alpha$ -pinene. *Microporous Mesoporous Mater.* **2012**, *163*, 237–242. [[CrossRef](#)]
48. Chen, H.P.; Xie, Y.P.; Chen, W.; Xia, M.W.; Li, K.X.; Chen, Z.Q.; Chen, Y.Q.; Yang, H.P. Investigation on co-pyrolysis of lignocellulosic biomass and amino acids using TG-FTIR and Py-GC/MS. *Energy Convers. Manag.* **2019**, *196*, 320–329. [[CrossRef](#)]
49. Viscardia, R.; Barbarossa, V.; Maggi, R.; Pancrazzi, F. Effect of acidic MCM-41 mesoporous silica functionalized with sulfonic acid groups catalyst in conversion of methanol to dimethyl. *Energy Rep.* **2020**, *6*, 49–55. [[CrossRef](#)]
50. Ding, H.; Yu, S.B.; Wei, J.S.; Xiong, H.M. Full-color light-emitting carbon dots with a surface-state-controlled luminescence mechanism. *ACS Nano* **2016**, *10*, 484–491. [[CrossRef](#)]
51. Ye, H.L.; Shang, Y.; Wang, H.Y.; Ma, Y.L.; He, X.W.; Li, W.Y.; Li, Y.H.; Zhang, Y.K. Determination of Fe(III) ion and cellular bioimaging based on a novel photoluminescent silicon nanoparticles. *Talanta* **2021**, *230*, 122294. [[CrossRef](#)] [[PubMed](#)]
52. Qiu, L.M.; Xu, G.T. Peak overlaps and corresponding solutions in the X-ray photoelectron spectroscopic study of hydrodesulfurization catalysts. *Appl. Surf. Sci.* **2010**, *256*, 3413–3417. [[CrossRef](#)]
53. Qiu, L.M.; Zou, K.; Xu, G.T. Investigation on the sulfur state and phase transformation of spent and regenerated S zorb sorbents using XPS and XRD. *Appl. Surf. Sci.* **2013**, *266*, 230–234. [[CrossRef](#)]
54. Bittencourt, C.; Hecq, M.; Felten, A.; Pireaux, J.J.; Ghijsen, J.; Felicissimo, M.P.; Rudolf, P.; Drube, W.; Ke, X.; Van, T.G. Platinum-carbon nanotube interaction. *Chem. Phys. Lett.* **2008**, *462*, 260–264. [[CrossRef](#)]
55. Chen, F.T.; Huang, Y.P.; Mi, C.J.; Wu, K.; Wang, W.Y.; Li, W.S.; Yang, Y.Q. Density functional theory study on catalytic dehydrogenation of methylcyclohexane on Pt (111). *Int. J. Hydrogen Energy* **2020**, *45*, 6727–6737. [[CrossRef](#)]
56. Miller, J.T.; Koningsberger, D.C. The origin of sulfur tolerance in supported platinum catalysts: The relationship between structural and catalytic properties in acidic and alkaline Pt/LTL. *J. Catal.* **1996**, *162*, 209–219. [[CrossRef](#)]
57. Ji, X.; Lee, K.T.; Holden, R.; Zhang, L.; Zhang, J.; Botton, G.A.; Couillard, M.; Nazar, L.F. Nanocrystalline intermetallics on mesoporous carbon for direct formic acid fuel cell anodes. *Nat. Chem.* **2010**, *2*, 286–293. [[CrossRef](#)]
58. Wang, L.; Chen, M.X.; Yan, Q.Q.; Xu, S.L.; Chu, S.Q.; Chen, P.; Lin, Y.; Liang, H.W. A sulfur-tethering synthesis strategy toward high-loading atomically dispersed noble metal catalysts. *Sci. Adv.* **2019**, *5*, eaax6322. [[CrossRef](#)]
59. Yin, P.; Luo, X.; Ma, Y.F.; Chu, S.Q.; Chen, S.; Zheng, X.S.; Lu, J.L.; Wu, X.J.; Liang, H.W. Sulfur stabilizing metal nanoclusters on carbon at high temperatures. *Nat. Chem.* **2021**, *12*, 3135. [[CrossRef](#)]
60. Chen, A.; Zhang, W.; Li, X.; Tan, D.; Han, X.; Bao, X. One-pot encapsulation of Pt nanoparticles into the mesochannels of SBA-15 and their catalytic dehydrogenation of methylcyclohexane. *Catal. Lett.* **2007**, *119*, 159–164. [[CrossRef](#)]
61. Wang, W.Y.; Miao, L.; Wu, K.; Chen, G.L.; Huang, Y.P.; Yang, Y.Q. Hydrogen evolution in the dehydrogenation of methylcyclohexane over Pt/Ce-Mg-Al-O catalysts derived from their layered double hydroxides. *Int. J. Hydrogen Energy* **2019**, *44*, 2918–2925. [[CrossRef](#)]
62. Yang, X.; Song, Y.; Cao, T.T.; Wang, L.; Song, H.T.; Lin, W. The double tuning effect of TiO<sub>2</sub> on Pt catalyzed dehydrogenation of methylcyclohexane. *Mol. Catal.* **2020**, *492*, 110971. [[CrossRef](#)]
63. Li, X.Y.; Ma, D.; Bao, X.H. Dispersion of Pt catalysts supported on activated carbon and their catalytic performance in methylcyclohexane dehydrogenation. *Chin. J. Catal.* **2008**, *29*, 259–263. [[CrossRef](#)]